Lawrence Livermore National Laboratory

Final Report: Mapping Fracture Network Creation with Microseismicity During EGS Demonstrations

Dennise C. Templeton, Eric Matzel, Gardar Johannesson, Stephen C. Myers, and Meredith Goebel

Unclassified

April 18, 2014
LLNL-TR-773974

Disclaimer

This document was prepared as an account of work sponsored by an agency of the United States government. Neither the United States government nor Lawrence Livermore National Security, LLC, nor any of their employees makes any warranty, expressed or implied, or assumes any legal liability or responsibility for the accuracy, completeness, or usefulness of any information, apparatus, product, or process disclosed, or represents that its use would not infringe privately owned rights. Reference herein to any specific commercial product, process, or service by trade name, trademark, manufacturer, or otherwise does not necessarily constitute or imply its endorsement, recommendation, or favoring by the United States government or Lawrence Livermore National Security, LLC. The views and opinions of authors expressed herein do not necessarily state or reflect those of the United States government or Lawrence Livermore National Security, LLC, and shall not be used for advertising or product endorsement purposes.

Auspices Statement

This work performed under the auspices of the U.S. Department of Energy by Lawrence Livermore National Laboratory under Contract DE-AC52-07NA27344.

Table of Contents

1   Introduction

Effective enhanced geothermal system (EGS) sites require optimal fracture networks for efficient heat transfer between hot rock and fluids. Microseismic mapping is a key tool used to infer the subsurface fracture geometry and is widely used in the petroleum industry to monitor fracture propagation during hydraulic stimulations. Traditional earthquake detection techniques (e.g. STA/LTA detectors) and location techniques are often employed to identify microearthquakes in geothermal regions. However, most commonly used algorithms may miss events if the seismic signal of an earthquake is small relative to the background noise level or if a microearthquake occurs within the coda of a larger event. Consequently, we have developed a set of algorithms that provide improved microearthquake detection even in difficult signal processing environments.

One such environment is the Newberry EGS reservoir which was stimulated by AltaRock Energy Inc. by injecting water into Well NWG 55-29, located on the eastern flank of the Newberry Volcano near Bend, Oregon. The injection program to date consists of 3 discrete stimulation periods, the first of which began October 16, 2012 and the last of which concluded December 7, 2012. Currently, only the injection well has been drilled. To determine the location of any future production wells, the active regions of the subsurface reservoir must be accurately illuminated. One method to aid in the determination of the reservoir fracture network is by accurate detection and location of the microearthquakes associated with the stimulation.

To increase the number of detectable microearthquakes before, during, and after the Newberry EGS stimulations, we apply the Matched Field Processing (MFP) earthquake detection algorithm to the to the continuous seismic data. The original earthquake catalog identified 234 events. The MFP technique identified 166 additional events during the same time period, or approximately 70% more events.

For the events with the highest signal-to-noise ratio (SNR) we apply MicroBayesLoc, a Bayesian multiple-event seismic location algorithm that allows for the determination of robust and realistic error estimates. This allows for the proper assessment of the uncertainty in the microearthquake locations to determine if observed spatial seismic features could in fact be artifacts of location uncertainty or true subsurface features.

A key component of microseismic event location is an accurate subsurface seismic velocity and attenuation model. A detailed image of the subsurface volume from the surface to just below the deepest zone of microseismic activity is necessary to effectively illuminate the reservoir volume. To accomplish this, we apply the ambient noise correlation (ANC) technique to dozens of seismic stations in and around the Newberry EGS site. Using a mix of instruments and networks, we maximize the resolution of the reservoir image both laterally and in depth. To verify the quality of our 3D model, we

compare synthetic seismograms calculated through the 3D model to observed seismic waveforms. Our results show that synthetic seismograms using the 3D velocity model better match the observed complexity of the direct and scattered waves than seismic energy propagated through the original 1D model.

This improved knowledge of the reservoir network will increase our understanding of subsurface conditions and allow improvement of the stimulation strategy and production well locations that will optimize heat extraction and maximize resource production.

2   Newberry EGS Seismic Network

The AltaRock Energy Phase 2 Newberry Microseismic Network consists of 8 2-Hz 3-component Oyo Geospace HS-1 borehole geophones and 7 2-Hz 3-component Oyo Geospace HS-1 buried surface geophones (Figure 1, Table 1). Additionally, Lawrence Livermore National Laboratory (LLNL) deployed 7 1-Hz 3-component Geotech GS-13 buried surface seismometers (Figure 1, Table 1).
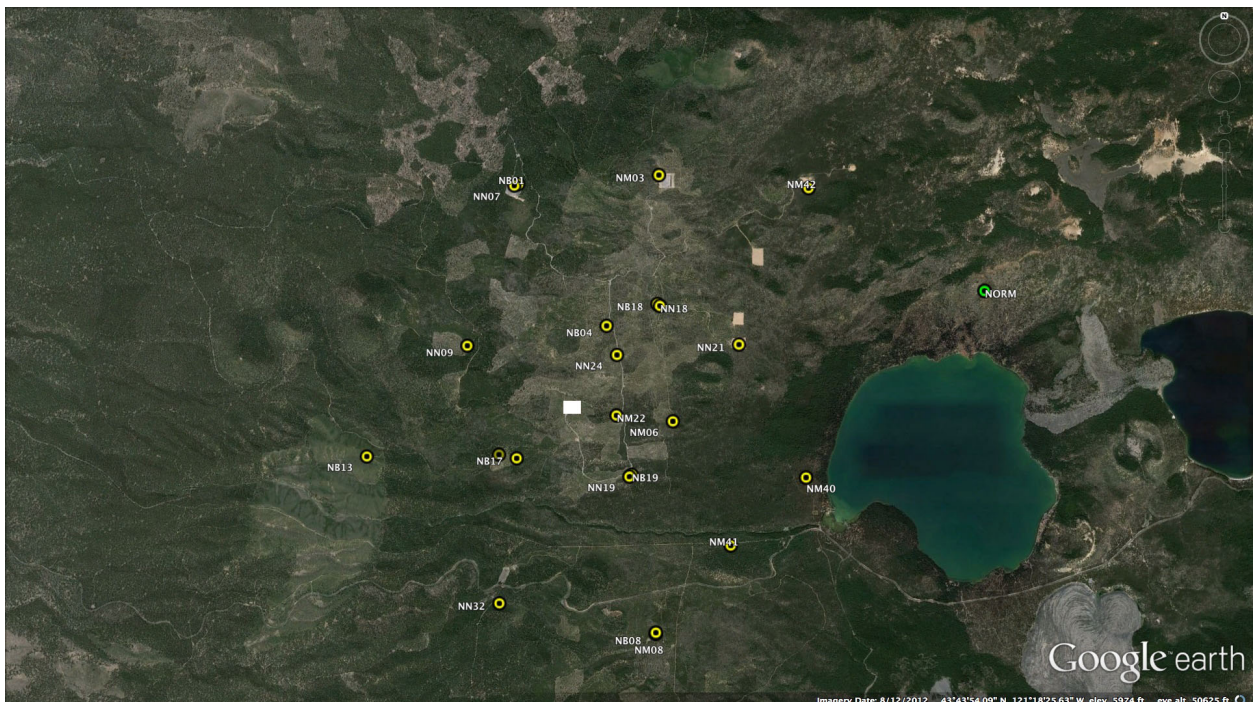

Figure 1. Map of Newberry caldera and vicinity showing locations of AltaRock Energy Inc. Phase 1 and Phase 2 seismometers as yellow circles. The white square at the center of the array indicates the location of the Well NWG 55-29 pad.

Station Name	Setting	Sensor	Recorder	Group
NM03, NM06, NM08, NM22, NM40, NM41, NM42	Surface	2-Hz Geospace HS-1	Geotech SMART-24R	A_1
NN07, NN09, NN17, NN18, NN19, NN21, NN24, NN32	Borehole	2-Hz Geospace HS-1	Geotech SMART-24R	A_2
NB01, NB04, NB08, NB13, NB18, NB19	Surface	1-Hz Geotech GS-13	Geotech SMART-24R	B
NB17	Surface	1-Hz Geotech GS-13	Guralp CMG-DM24-S3	C

Table 1. Seismic instrumentation deployed at the Newberry EGS site.

3   Original Earthquake Catalog

We use a merged combination of the Foulger Consulting earthquake catalog (Foulger and Julian, 2013) and the Lawrence Berkeley National Laboratory (LBNL) Newberry EGS online catalog as the original earthquake catalog for this study (Figures 2 and 3). Between October 17, 2012 and February 18, 2013, the Foulger Consulting catalog is considered to be the primary authoritive catalog with 227 microearthquakes.

The LBNL online catalog is updated in real-time, and as such spans a longer time period, however it is expected to have greater errors than the Foulger Consulting earthquake catalog. We use the LBNL catalog primarily to fill in the time gap between the end of the Foulger Consulting catalog and the end of the current study period on September 30, 2013. We use 7 events from the LBNL catalog that occur within the footprint of the Newberry EGS microseismic array during the duration of the study. The last event in the LBNL catalog occurs on June 28, 2013. The total number of events in our merged Foulger Consulting – LBNL catalog is 234.

Although the stimulation started on October 16, 2012, the first catalog event occurred on October 29, 2012. No microseismic events were originally identified pre-stimulation.
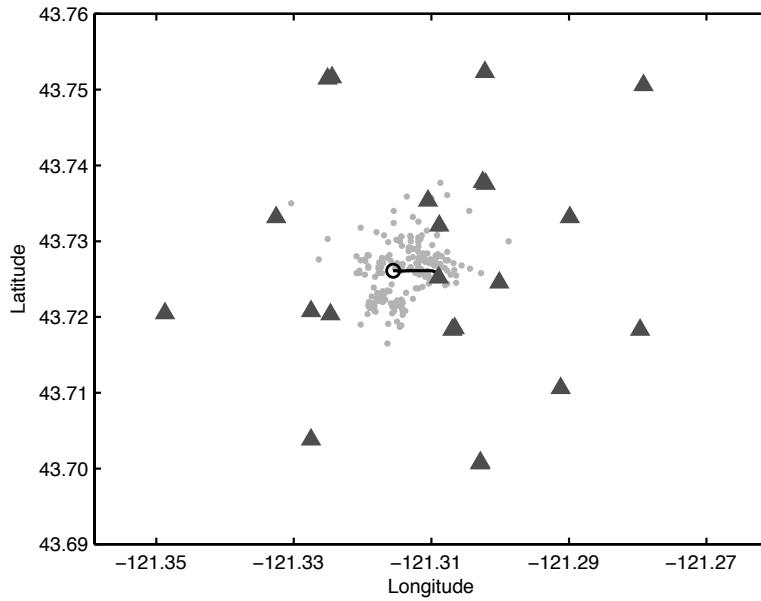
Figure 2. Map view of original catalog events occurring between October 1,2012 and September 30, 2013 plotted as light grey dots. Seismic stations are indicated by dark grey triangles, the surface location of the stimulation well is indicated by the black open circle and the black line indicates the deviation of the well with depth.
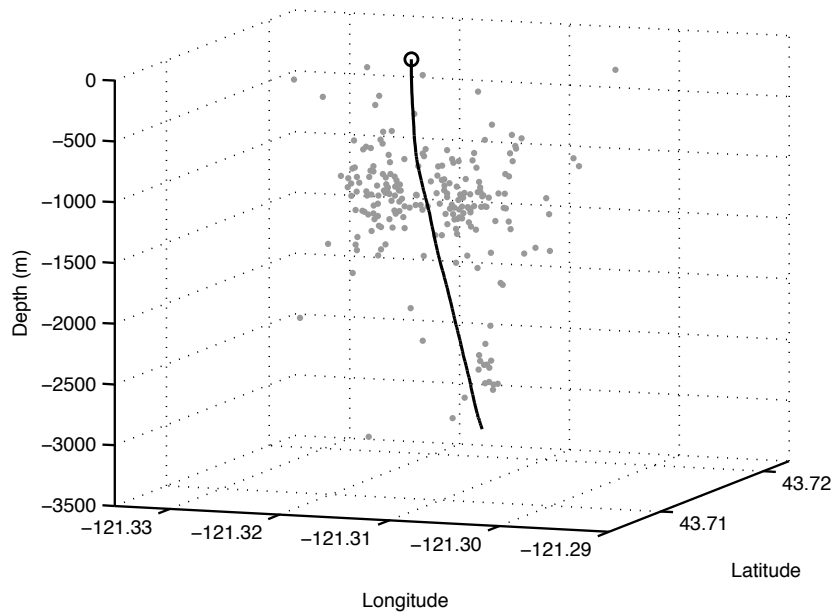

Figure 3. Depth view of original catalog events occurring between October 1, 2012 and September 30, 2012 plotted as grey dots. The surface location of the stimulation well is indicated by the black open circle and the black line indicates the location of the wellbore with depth.

3.1 Verification of Original Earthquake Catalog

To verify the effectiveness of the original earthquake detection technique, we run a standard STA/LTA earthquake detection routine on the Newberry continuous seismic data. The STA/LTA detection method detects seismic events by comparing the average of the signal over a short time period (short time average or STA) to the average signal over a longer period (long term average or LTA). During an event this ratio will increase significantly. The user can decide on trigger and detrigger values that allow the STA/LTA method to recognize the beginning and end of an event. There are multiple ways to calculate the long term and short term averages (recursively, fixed values, classic, ect.). For more details see Trnkoczy (2002).

Events were originally detected by AltaRock Energy Inc. using the SMARTQuake program. This program utilized a phase detector based STA/LTA based on the Allen [1978] algorithm, which calculates the amplitude value within the short term window and the long term window using a characteristic function. In this method, triggering is sensitive to both amplitude and frequency changes. SMARTQuake also discriminates local/distant events using a user inputted time window for determining predominant signal frequency and a threshold for discrimination (Hz). If the median value of the predominant signal frequency is above the threshold value (3 Hz in this and most cases) then the event is considered local, if it is lower then it is considered to be a distant event. SMARTQuake allows the user to specify the number of triggered traces needed to record a trigger, but not the short or long term window length.

To verify the SMARTQuake catalog, we created a recursive STA/LTA coincidence trigger program using the ObsPy Python module. We used a 0.1 sec STA window, a 25 sec LTA window, 17 as the trigger threshold, and 4.5 +/- 1.5 sec as the detrigger threshold, the value of which depended on the general noise level of the seismogram. Triggers were then visually inspected to verify that they were real events. Verification was conducted by looking at both the ground motion and frequency content plots of the event to verify that a local event with high frequency content and of short duration had occurred.

There was substantial overlap in the number of events triggered by both methods, however the LLNL STA/LTA program identified 28 new events, or approximately 10% more events, not previously identified by the original earthquake detection program.

4 Identification of More Microearthquakes Using MFP

4.1 MFP Earthquake Detection

Our MFP technique differs from the established earthquake detection techniques in that it is a template matching formulation. It is an adaptation of a signal processing technique originally

developed to locate continuous underwater acoustic sources [Bucker 1976; Baggeroer *et al.* 1993]. We calculate the wavefield structure of a known event with high signal-to-noise ratio across an array by estimating the structure directly from field calibration data, i.e., previously observed seismic events. These master templates contain contributions from both direct and scattered seismic energy. The MFP technique breaks the signals into a large number of narrow frequency bands, processes the narrow band signals such that they are approximately independent from each other, performs the matching operation band by band, and combines the results incoherently across the bands.

MFP largely eliminates the sensitivity of correlation matching operations to source time history variations by processing the observed data stream in a large number of narrow frequency bands. This makes MFP sensitive to the spatial structure of the signal at the observing aperture (controlled by mechanism and propagation), but not the temporal structure (controlled, in part, by source time history). In this way MFP can identify previously undiscovered events even if they bear little resemblance to the master event in the time domain. The trade off is that the origin times of the new events have errors on the order of seconds and thus must be independently determined.

4.2   Creation of Master Matching Templates

Master templates are created from master events. They are used to identify new events in the seismic datastream. The master events are selected based on two criteria. First, calibration events cannot be superimposed on other events on the seismic record. Second, waveforms of master events must also have high signal-to-noise ratios (SNR), especially in the lower frequency ranges, on at least four three-component seismic stations. No other selection criteria based on magnitude, mechanism or location is taken into consideration. Using these criteria, we investigated all catalog events as potential master events. We identify 78 events out of the original 234 catalog events that could be employed as master events (Figure 4).
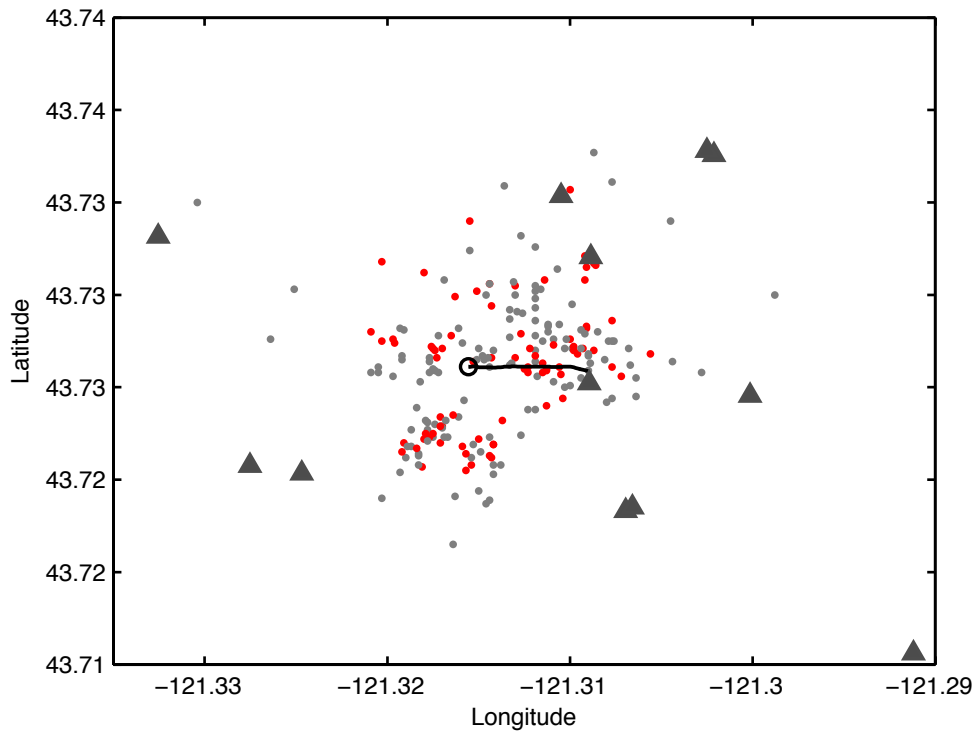
Figure 4. Close up map view showing master events in red and non-master events in grey. Seismic stations are indicated by grey triangles, the surface location of the stimulation well is indicated by the black open circle and the black line indicates the deviation of the well with depth.

4.3   Application of MFP Methodology to the Continuous Seismic Data

The MFP code compared master templates to the continuous seismic data using a 21-sec sliding window that stepped forward at 1-second intervals. Comparisons between master events and new data were performed in the 6 – 12 Hz frequency band for continuous data between September 1, 2012 and September 30, 2013.

The original catalog reported 234 events between October 17, 2012 and September 30, 2013. The MFP earthquake detection code was able to identify 166 additional events (Figures 5 and 6). Newly detected events were given preliminary locations matching that of the master event that identified it.

An example of a newly detected event is shown in Figure 7. Notice how different noise sources obscure the signal in the time domain, but that the event can be identified more clearly in the frequency domain.
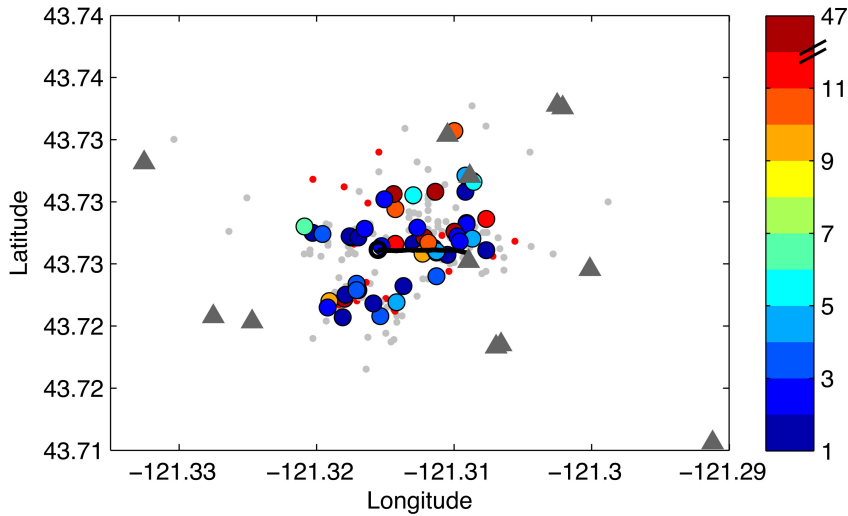
Figure 5. Close up plot in map view showing the location of the newly detected events as circles color coded to indicate the number of new events detected at each location. Master events that did not detect any new events are plotted as red dots. Catalog events that were not used as master events are plotted as grey dots. Seismic stations are indicated by grey triangles, the surface location of the stimulation well is indicated by the black open circle and the black line indicates the deviation of the well with depth.
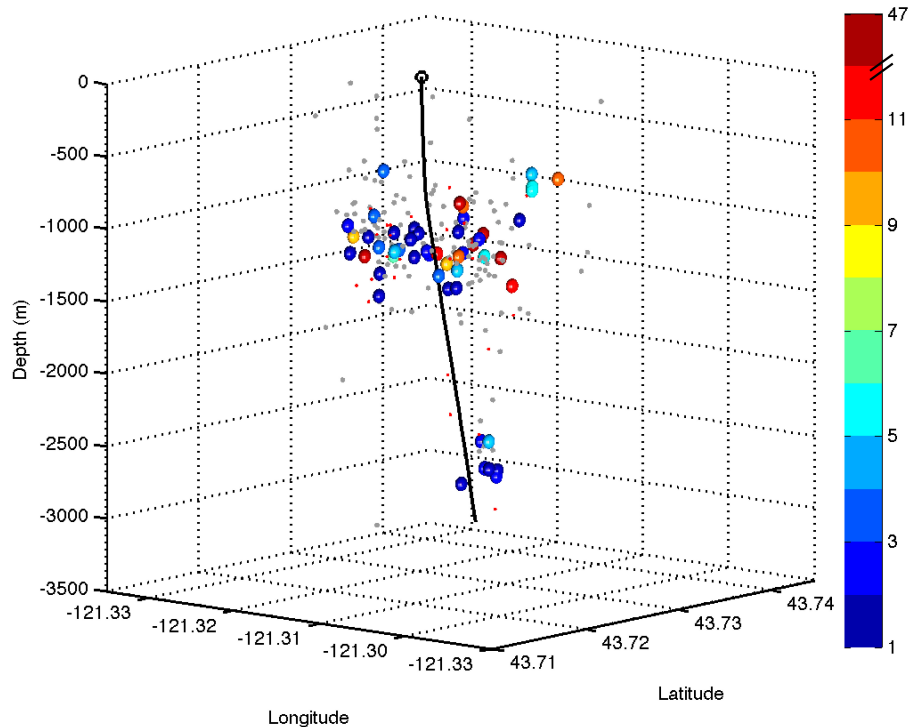

Figure 6. Plot in depth view showing newly detected events as spheres. The circles are color coded to indicate the number of new events detected at each location. Catalog events that were designated as a master event but did not identify any new events are plotted as red dots. Catalog events that were not used as master events are plotted as grey dots.
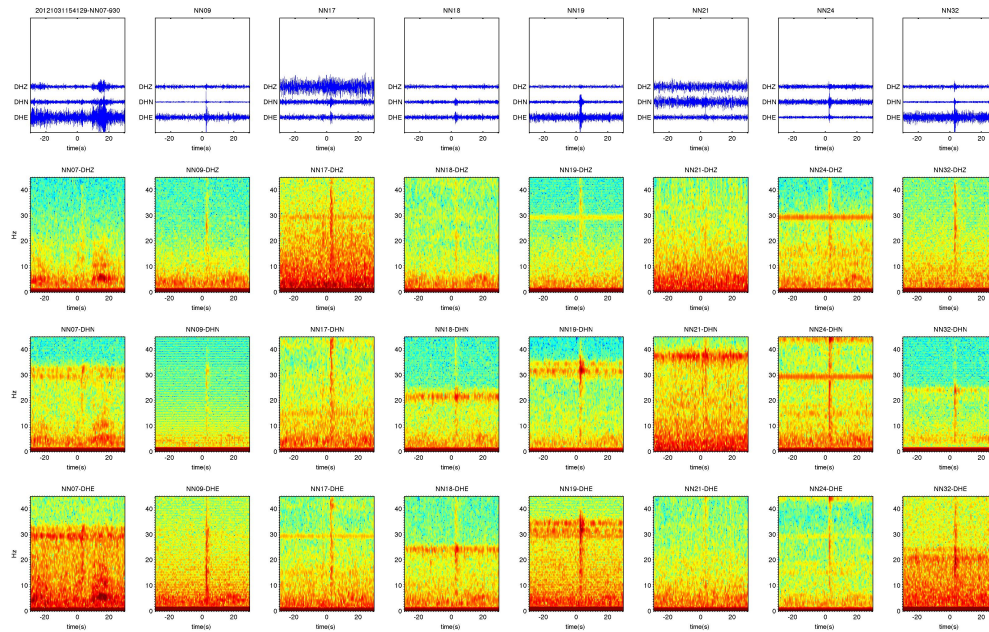
Figure 7. Example of a newly detected event not in the original catalog. Each column contains plots for one station. The first row shows the event in the time domain. The second, third and fourth rows show spectrograms of the vertical and horizontal components between 0 − 45 Hz.

Only one additional event was identified that occurred pre-stimulation. This event occurred on October 1, 2012 and was located in the shallow seismic zone (Figure 8). Additionally, one other event was detected post-stimulation, but before the first event in the official catalog. This event occurred on October 20, 2012 and was also located in the shallow seismic zone (Figure 8). No other events were detected between September 1, 2012 and October 28, 2012.
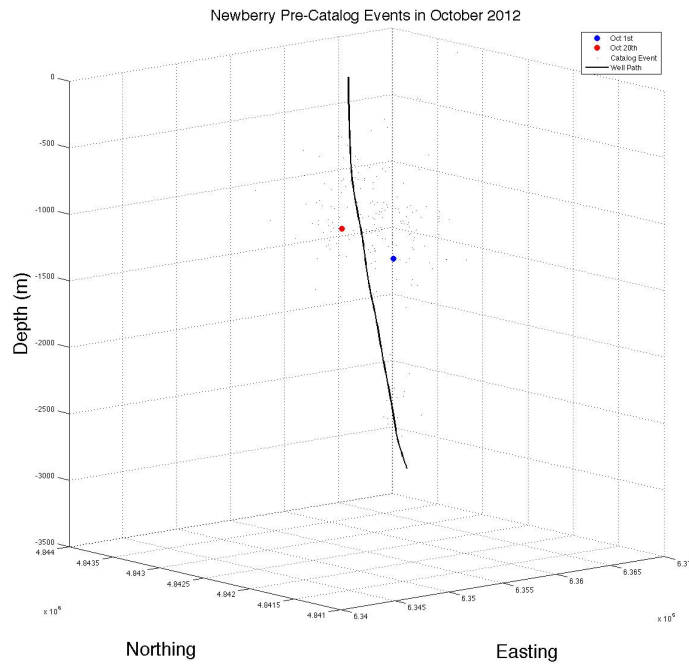
Figure 8. Plot in depth view showing the location of the October 1 pre-stimulation event in blue and the October 20 pre-catalog event in red.

4.4   Determination of New Event Magnitudes

Duration magnitudes, Md, were determined for the newly identified events (Figure 9). This was accomplished by first determining an average event duration from the vertical components of original catalog events for which there was a P pick and for which there was not another known event within 5 seconds. A linear best fit between the log_{10} event durations and the original catalog event moment magnitude was calculated. This model was then used to determine duration magnitudes for new events based on their measured event duration.

Figure 9. Comparison of the magnitudes of events in the original earthquake catalog, in dark grey, with the magnitude of new events, in light grey. In general, new events tended to be smaller microearthquakes.

5   MicroBayesloc Event Relocation

We locate multiple microseismic events simultaneously following the Bayesian methodology originally implemented in the global-scale Bayesian multiple e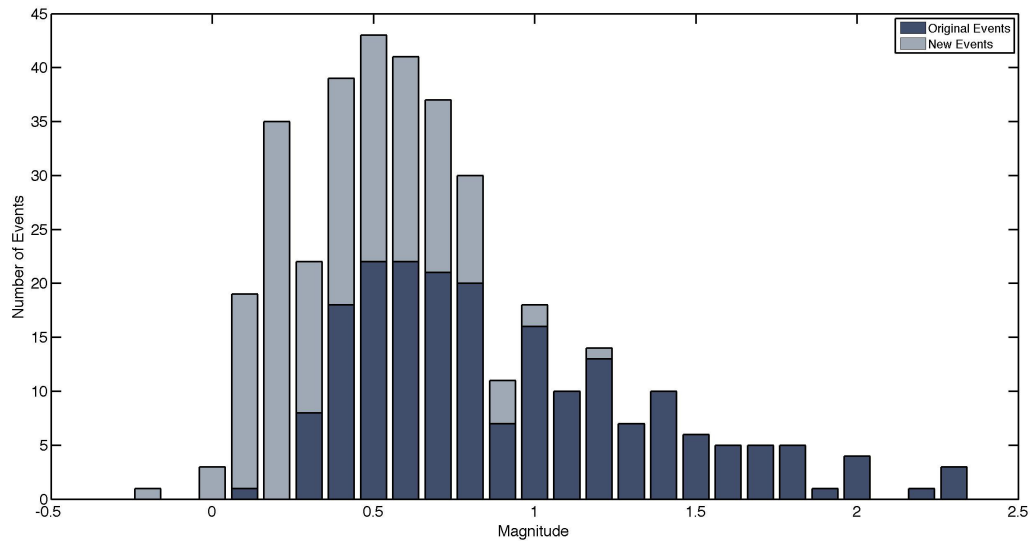vent seismic locator, BayesLoc (Myers et al., 2007). This Bayesian methodology allows for probabilistic constraints on any combination of the arrival-time data, the travel time model, and the location parameters. Sampling from the resulting Bayesian posterior distribution is accomplished using the Markov Chain Monte Carlo (MCMC) method.

We assume a relatively simple travel-time model for P arrivals based on a linear change in velocity with depth. A 'tuning' parameter for the earth model in the multiple microseismic event location problem is adjusted as part of the Bayesian location problem to yield the best match to the observed data. At the core of the Bayesian locator is a statistical model that links observed data to unobserved parameters through the earth model. The statistical model consists of three main components: (1) a prior probability model for the source parameters in 3D location and time, (2) a statistical model for the correction to the assumed earth model (i.e., the travel-time corrections), and (3) a statistical model for the error in the observed data (e.g., the spread of the arrival-time residuals).

For the Newberry EGS data set, we chose a subset of 199 events with 1441 P picks and 1267 S wave picks. The pick catalog was obtained from AltaRock Energy Inc. Figure 10 shows the posterior marginal

densities of the three travel-time parameters. Figure 11 shows the 3D locations of the 199 events along with the receiver locations. The event locations are colored according to their estimated accuracy, represented by the volume of the 95% ellipsoid.

Investigation as to the cause of the relatively large uncertainty of the deeper events showed that relatively small errors in the S-wave picks were the influencing the size of the 95% ellipsoid volume. A test using a small subset of events in which the P- and S-wave energy was rotated to better isolate the S-wave particle motion for improved picking accuracy showed a significant decrease in the size of the ellipsoids (Figure 12). Future work will focus on this area.
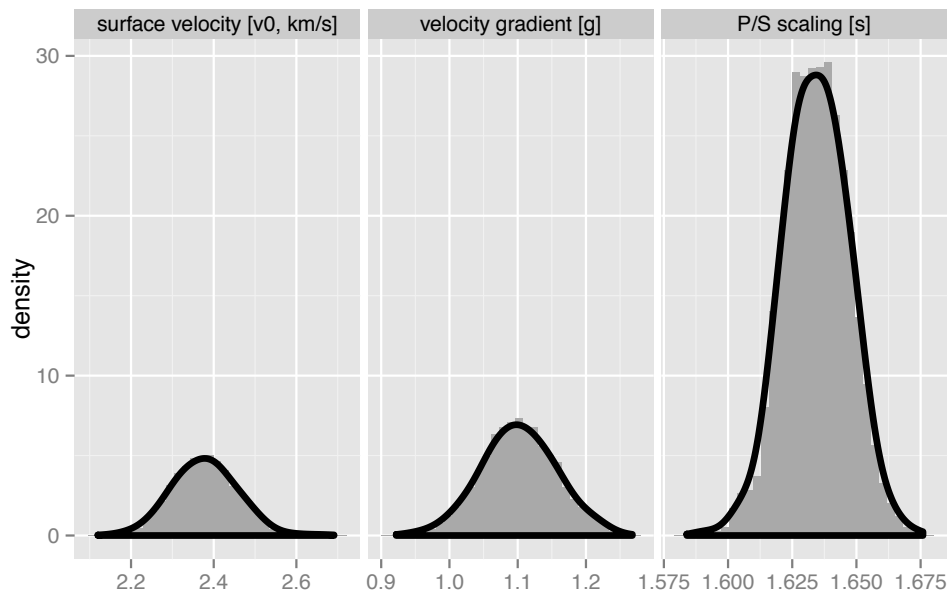
Figure 10. The posterior histogram of the three travel-time model parameters (surface velocity, gradient, and P/S scaling parameter) for the Newberry EGS dataset.
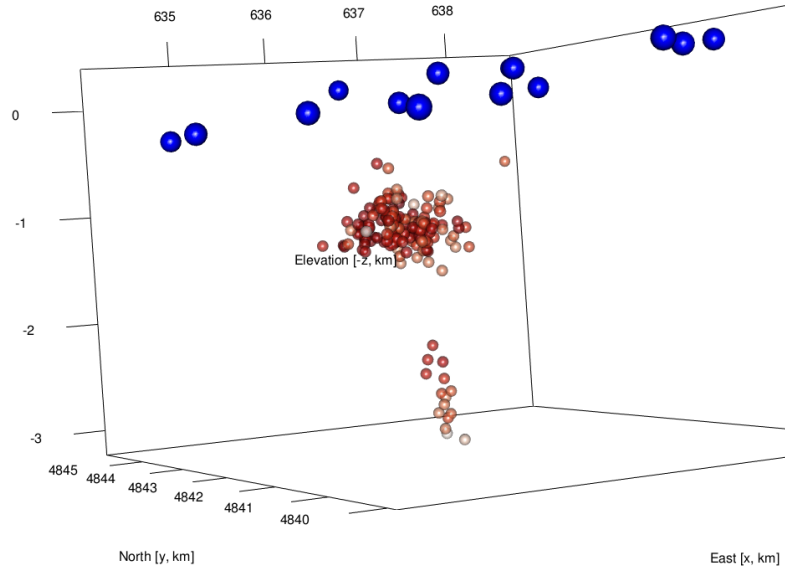
Figure 11. Depth view of event locations colored according to their estimated accuracy, represented by the volume of the 95% ellipsoid. Darker colors are indicative of greater accuracy. The station locations are indicated by the blue circles.
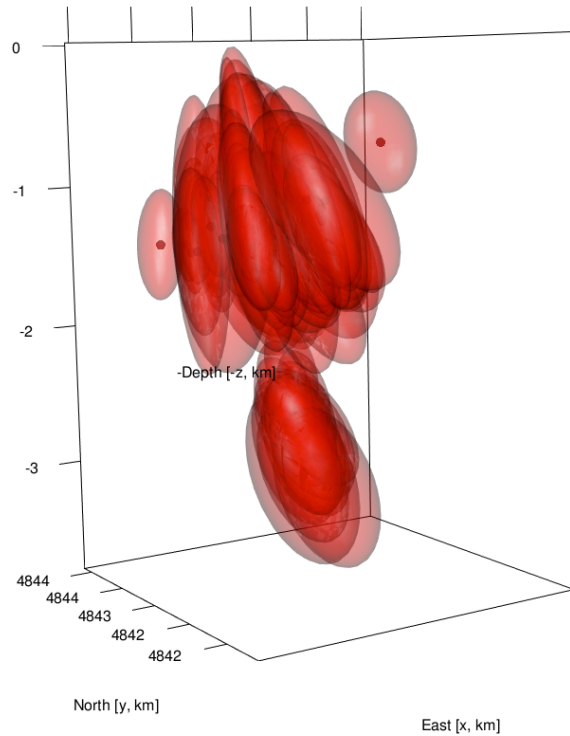
Figure 12. Depth view of event locations posterior mean as the dark red circle and their 95% ellipsoids. Although the vertical errors are significantly larger than the horizontal errors, primarily due to the recording station geometry, the errors are such that the two seismic swarms are most likely occurring in distinct regions of the reservoir.

6   Creation of 3D Velocity Model

Ambient noise correlation (ANC) is a technique in which the data recorded at one seismometer are correlated with the data recorded at another to obtain an estimate of the Green's function (GF) between the two. The cross correlation of ambient noise between a pair of stations results in a waveform that is identical to the seismogram that would result if an impulsive source located at one of the stations was recorded at the other. Because of this, the techniques developed for earthquake seismology can be applied to the correlations themselves.

Using ANC, we created a 3D model of the Newberry site down to a depth of 5km. We collected continuous data for the month of October 2012, for the 22 stations in the Newberry network, together with 12 additional stations from the nearby CC, UO and UW networks. The data were instrument corrected, whitened and converted to single bit traces before cross correlation according to the methodology laid out in Benson (2007).

There are 231 unique paths connecting the 22 stations of the Newberry network. The additional networks extended that to 402 unique paths crossing beneath the Newberry site. Because we are particularly interested in the very shallow seismic structure, we need high quality correlation waveforms at frequencies from 0.5-15 Hz. These particular data are very good and the GFs emerged quickly.

We treated each GF as a seismic record and inverted for the best fitting 1D model along each path. The objective function was to maximize the fit between the GF and synthetic seismograms, including the scattering energy in the coda. Short paths and high frequencies are most sensitive to the shallowest structures. Deeper structures are resolved for longer paths. We inverted simultaneously for Vp, and Vs and Qs, although Qs is poorly resolved. We broke the data into 3 groups. GFs for paths shorter than 5 km were filtered between 0.6 to 15 Hz and focused on matching details to 1 km. For paths between 5 - 10 km we filtered GFs between 0.5-8 Hz and data for the longest paths were filtered between 0.1 - 2 Hz. These longest paths, typically including at least one station outside the Newberry network, extended our depth coverage below 5km.

The individual 1D models were merged into a tomogram of the region using singular value decomposition. Two slices through the final 3D model are presented in Figure 13. Note how the seismicity generally follows the rapid change in velocity gradient between the highs and lows. This remarkable feature can be seen in most of the 2D slices throughout the model.
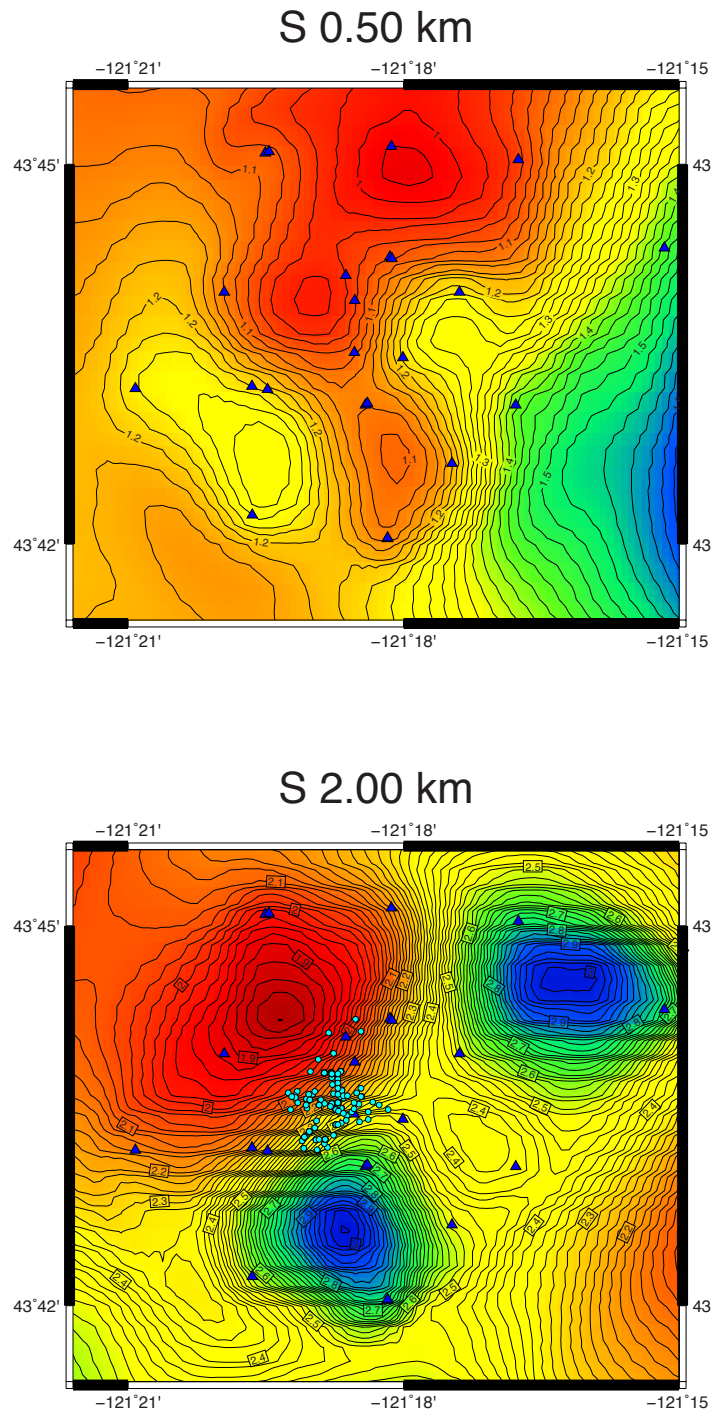
Figure 13. Slices through the shear velocity model at 0.5 and 2.0 km depth, including the independently located seismicity (cyan circles). Continuous data from Newberry network stations (blue triangles) and nearby seismic networks (off map) were used to constrain the velocity structure beneath the site down to 5 km.
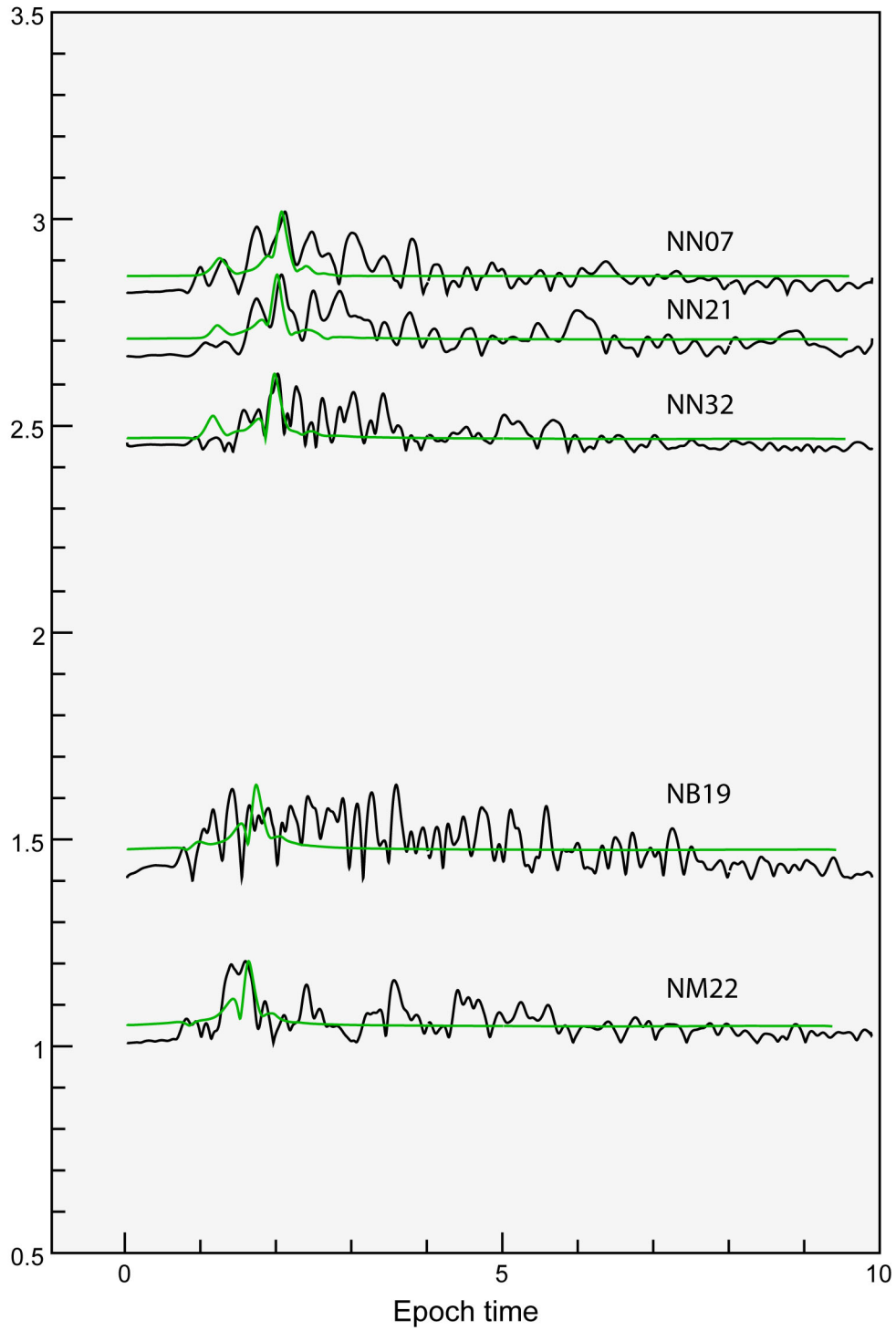
Figure 14. Envelopes of data for the 12/01/2012 event, recorded by the Newberry seismic network (black) compared to the synthetics calculated through reference 1D model (green).
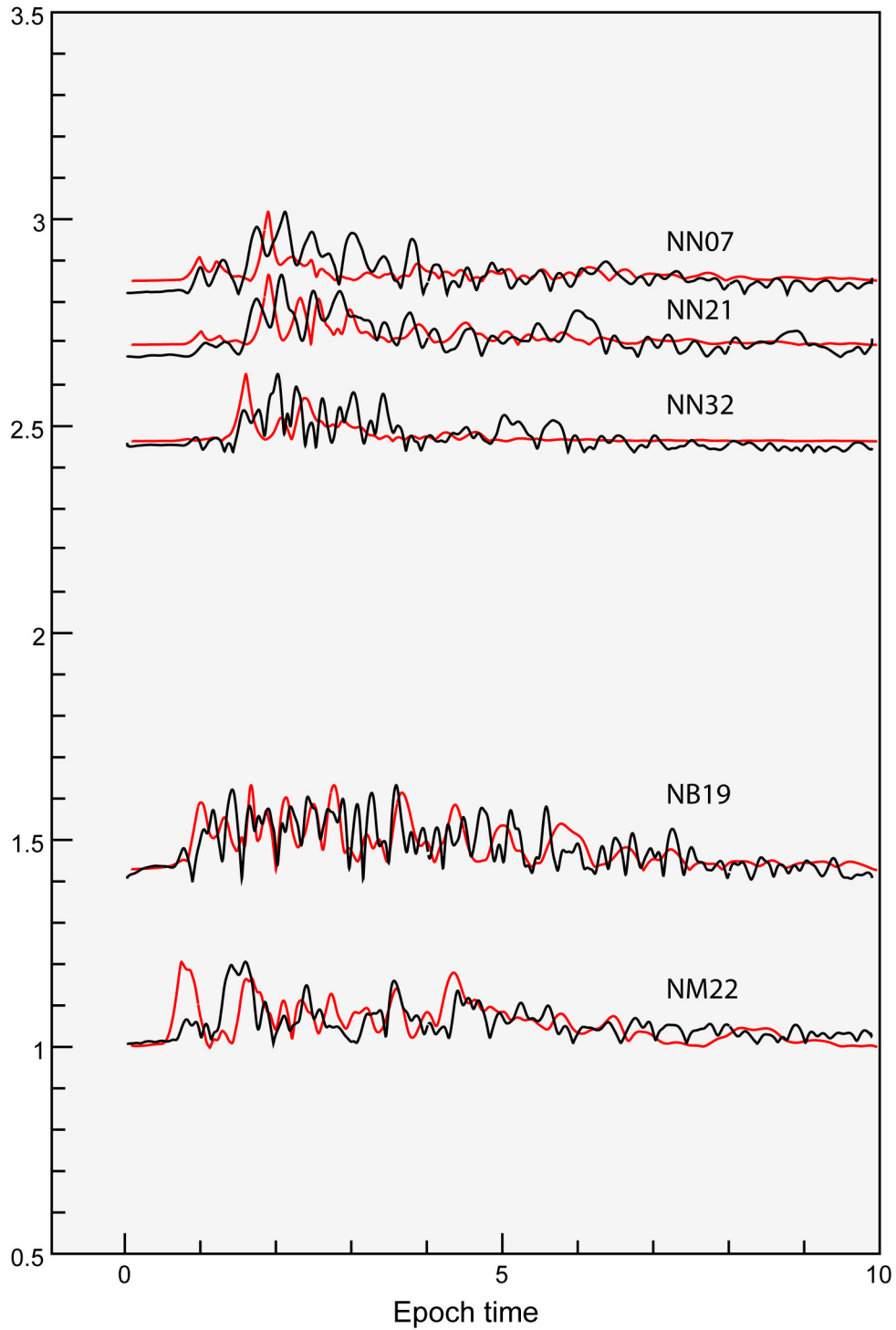
Figure 15. Envelopes of data for the 12/01/2012 event (black) and synthetics (red) calculated through the 3D model. Notice the improvement in fit to the data compared to the 1D model, especially when modeling the surface waves at NB19.

To test the accuracy of the model, we calculated synthetic seismograms for local earthquakes through both the original 1D and 3D models using the reflectivity method and the LLNL SW4 code, respectively. We compare the synthetics to a M1.85 earthquake that occurred on December 1, 2012. For clarity, we plot a representative set of data and synthetic waveform envelopes calculated through the 1D model (Figure 14). Notice how the 1D synthetics are only able to capture one or two peaks of the actual wavetrain. Waveform envelopes of the data and synthetics calculated through the 3D model are compared in Figure 14. The 3D synthetics are able to accurately capture the complexity of the surface waves, such as those observed at the NB19 surface station (Figure 15). Discrepancies in the phase and amplitude between the data and 3D synthetics can be due to lack of resolution of the current parameters, such as problems with the estimated Q value, or indicate a need for a longer time span of data. Refinements to the model based on comparisons such as these are expected to improve the overall robustness of the 3D velocity model.

7   Comparison Between Seismicity and Injection Data

7.1   Daily Rates

We plot the number of seismic events per day compared to the daily injected volume and the daily average well head pressure (Figure 16). There is a general relationship between the amount of fluids injected and the number of seismic events per day, however the seismicity appears to be sometimes delayed from the peak in the fluid parameters. Although the stimulation began on Day 290, seismicity did not occur with great frequency until approximately 2 weeks later when the daily injected volume and the average well head pressure reached a peak. Although no events were originally recorded during a small air injection occurring near Day 350, several extremely small microearthquakes were identified using the MFP technique (Figure 16).
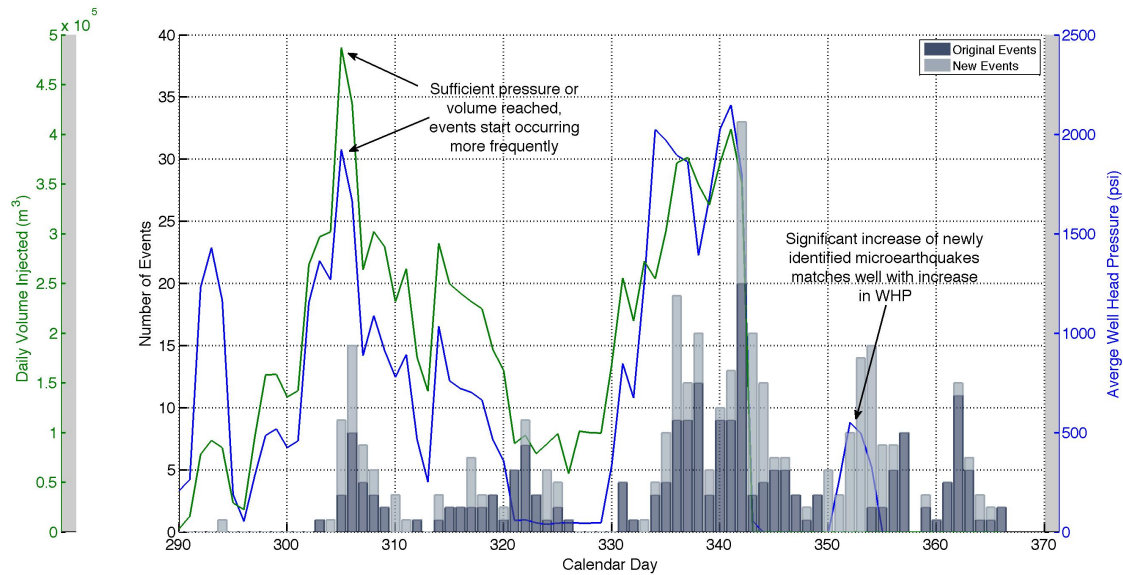
Figure 16. Comparison of the daily number of seismic events, the daily injected volume, and the daily average well head pressure. The number of original catalog events are plotted in dark grey and the number of newly detected events are plotted in light grey. The daily injected volume is plotted in green and the daily average well head pressure is plotted in blue.

8   Conclusions

We performed a standard STA/LTA earthquake detection routine to verify the suitability of the AltaRock automatic STA/LTA parameters. We verified that the original STA/LTA parameters were appropriate, although the LLNL STA/LTA program identified 28 new events, or approximately 10% more events, not previously identified by the original earthquake detection program. There were 234 events in the original merged earthquake catalog during this same time period.

Additionally, using the MFP method, we were able to identify 166 more events, or approximately 70% more events, occurring between September 1, 2012 and September 30, 2013 at the Newberry EGS site. These new events occurred primarily in the shallower seismic zone. We applied the MFP technique to high quality continuous data from 8 borehole sensors in the Newberry microseismic array that have the best overall signal to noise ratio. The new events tended to be of smaller magnitude than the events that were detected using standard earthquake detection techniques.

A comparison between the total number of seismic events per day and the daily injected volume and the daily average well head pressure shows that there is a general relationship between the amount of fluids injected and the number of seismic events per day. However, the seismicity appears to be often

slightly delayed from the peak in the fluid parameters. This is seen even at the beginning of the stimulation. Seismicity (both original and newly detected) only occurred infrequently until approximately 2 weeks after the start of the stimulation when the daily injected volume and the average well head pressure reached a peak.

The MicroBayesLoc multiple-event locator accurately characterized the uncertainty associated with the seismic data and model. MicroBayesLoc seismic event locations showed that although the location errors were larger in the vertical direction, primarily due to the relatively small aperture of the seismic recording stations, the locations delineated two distinct regions within the reservoir that were activated and illuminated by the upper and lower seismic swarm. Testing indicated that the vertical errors could be decreased by increasing the accuracy of the S-wave picks by rotating the seismograms before phase picking.

We applied ANC to dozens of seismic stations in and around the Newberry EGS site to determine the 3D velocity model. We demonstrated that the mix of instruments and networks maximized the resolution both laterally and with depth. Synthetic seismograms calculated through the 3D model were able to capture more of the complexity of the direct and scattered waves that are observed in the microearthquake data than were synthetic seismograms calculated using the 1D model. An increase in the accuracy of the velocity model can reduce the magnitude of the earthquake location errors and increase the resolution of the subsurface seismic delineations.

9 References

Allen, R., (1978). Automatic earthquake recorgnition and timing from single traces. *Bull. Seismol. Soc. Am.,* 68, 1521 – 1532.

Asch, G. (2009). Seismic Recording Systems, in P. Bormann (Ed.), *New Manual of Seismological Observatory Practice (NMSOP)*, Potsdam: Deutsches GeoForschungsZentrum GFZ, 1 – 20.

Baggeroer, A.B., W. A. Kuperman, P.N. Mikhalevsky (1993). Matched field processing in ocean acoustics, in J.M.F. Moura and I.M.G Lourtie (Eds.), *Proceedings of the NATO Advanced Study Institute on Signal Processing for Ocean Exploration,* Kluwer, Dordrecht, Netherlands.

Benson, G.D., M.H. Ritzwoller, M.P. Barmin, A.L. Levshin, F. Lin, M.P. Moschetti, N.M. Shapiro, and Y. Yang (2007). Processing seismic ambient noise data to obtain reliable broad-band surface wave dispersion measurements, *Geophys. J. Int,* 169, 1239-1260

Bucker, H.P. (1976). Use of calculated sound field and matched-field detection to locate sound sources in shallow water, *J. Acoust. Soc. Am.,* 59, 368 – 373.

Eaton, J.P. (1975). Harmonic Magnification of the Complete Telemetered Seismic System, from Seismometer to Film Viewer Screen, U.S. Geol. Surv. Open-File Report 75-99, 40 pages.

Foulger, G. R., and B. R. Julian (2013). Report to AltaRock Energy Inc.: Earthquake Seismicity Associated with the Newberry EGS Demonstration, March 18, 2013.

Healy, J.H., and M.E. O-Neill (1977). Calibration of Seismographic Systems: USGS Stations in the Central California Network, U.S. Geol. Surv. Open-File Report 77-736, 176 pages.

Myers, S.C., G. Johannesson, W. Hanley (2007). A Bayesian hierarchical method for multiple-event seismic location, Geophys. J. Int., 171, 1049-1063.

Scherbaum, F. (2001). Of Poles and Zeros: Fundamentals of Digital Seismology, Dordrecht: Kluwer Academic Publishers.

Trnkoczy, A. (2002). Understanding and parameter setting of STA/LTA trigger algorithm. In Bormann, P. (Ed.), *IASPI New Manual of Seismological Observatory Proctice, vol. 2.,* Geo Forschungs Zentrum Postdam, pp. 119.

Appendix A

Conversion of Seismic Data From Raw Counts to Physical Units

Determine Form of Transfer Function

To account for the distortion that seismic recording systems necessarily introduce into the ground motion signals they are measuring, the Laplace transform is applied to the equation of motion for the seismometer. In general, the Laplace transform converts a function from the time-domain to the frequency-domain, where the equations become functions of the complex angular frequency, s. Conceptually, we see that the Laplace transform of the output recorded signal, Y(s), is equal to the Laplace transform of the input true ground signal, X(s), multiplied by the Laplace transform of the transfer function, T(s):

$$Y(s) = T(s)X(s)$$

This transfer function can be specified using a variety of different parameters. Here we describe the transfer function using the poles and zeros of the transfer function together with a gain factor. Assuming that the seismic sensor can be represented using a simple mass, spring, and dashpot system, the velocity transfer function for the velocity sensors in this study can be written in the form

$$T_{vel-rad}(s) = \frac{Y(s)}{X(s)} = -c_{vel}\frac{-s^2}{s^2 + 2\beta\omega_0 s + \omega_0^2}$$

where $T_{vel-rad}(s)$ is the velocity transfer function in units of radians, c_{vel} is the frequency independent scale factor for the velocity form in units of V/m/s, β is the sensor total damping constant in percent of critical, and ω_0 is the natural frequency of the seismometer in radians (Scherbaum, 2011). The frequency independent gain factor is sometimes also referred to as the scale factor and has units of the sensor output signal units divided by input signal units (e.g., V/m/s for a velocity sensor). The frequency dependent portion is dimensionless.

ω_0, in radians, can be calculated using the natural frequency of the sensor, f_0, in Hz using the simple relationship

$$\omega_0 = 2\pi f_0$$

The sensor total damping constant, β, in units of percent of critical, is defined as

$$\beta = \beta_o + \beta_c$$

where β_o is the open circuit damping due to the mechanical properties of the sensor (usually provided on the sensor specification sheet) and β_c is the current damping due to the electrical properties of the sensor and datalogger. The current damping can be determined using

$$\beta_c = \frac{G_0^2}{2\omega_0 m R_t}$$

where G_0^2 is the instrinsic sensitivity of the velocity sensor in V/m/s (usually provided on the sensor specification sheet), m is the mass of the sensor in kg (usually provided on the sensor specification sheet), and R_t is the total resistance of the entire system in ohms. The total resistance can be determined using

$$R_t = R_c + R_{load}$$

where R_c is the feedback coil resistance in ohms (usually provided on the sensor specification sheet), and R_{load} is the parallel sum of all the parallel resistors in the system (e.g., a shunt resistor, a preamplifier or resistor, and/or a datalogger, Z_{amp}). In this study there were no series resistors installed in the seismic system, so we will ignore any possible contribution from series resistors in this formulation.

We installed a parallel external damping resistor, R_s, between the GS-13 seismic sensors and the digitizers to attenuate the signal. The appropriate value of the resistor was determined by

$$R_{s-theoretical} = \frac{CDR}{0.7} - R_c$$

where *CDR* is the instrument critical damping resistance in ohms at 1.0 Hz (provided on the sensor specification sheet), R_c is the main coil resistance in ohms (provided on the sensor specification sheet), and 0.7 indicates our choice of relative damping value. The actual resistors, R_s, were fabricated in the laboratory for each station with values as close as possible to $R_{s-theoretical}$.

In general, R_{load} can be determined for an arbitrary number of parallel resistors using the relationship

$$\frac{1}{R_{load}} = \sum_{x=1}^{n} \frac{1}{R_x}$$

In the special case where there may be only two resistors (e.g., a damping resistor and a datalogger), the following much simpler formula to find the resistance value is often used

$$R_{load} = \frac{R_s \cdot Z_{amp}}{R_s + Z_{amp}}$$

In the special case where there may be only one resistor (e.g., only a datalogger), R_{load} simplifies to

$$R_{load} = Z_{amp}$$

For passive electrodynamic sensors, such as the GS-13s, the input impedance of the datalogger should be at least 2 orders of magnitude larger than the total resistance of the disconnected sensor. If this is true, then the datalogger will not significantly influence the sensor electronics or change the damping and sensor poles. This is not an issue for active sensors since the input impedance of the recording device does not influence the sensor's characteristics (Asch, 2009).

Determine Poles and Zeros of Transfer Function

The poles of the transfer function are determined from the roots of the *T(s)* denominator. The zeros of the transfer function are the zeros in the T(s) numerator. In this case, we can see that for the velocity transfer function $T_{vel-rad}(s)$ there are two zeros at zero and for the displacement function $T_{disp-rad}(s)$ there are three zeros at zero.

For the underdamped case ($\beta < 1$), the poles for both velocity and displacement become

$$p_{1,2} = -\beta\omega_0 \pm i\omega_0\sqrt{1 - \beta^2}$$

where ω_0 is again the undamped seismometer eigenfrequency in radians and β the total sensor damping constant (Scherbaum, 2001).

Determine the Pole-Zero Constant

The pole-zero constants can be determined using

$$CONSTANT_{vel-rad} = A0_{vel-rad} * G_s * G_d$$

where $A0_{vel-rad}$ is the velocity normalization factors. The sensor gain, G_s, describes the effective sensitivity of the sensor. The digitizer gain, G_d, describes the sensitivity of the digitizer, in units of counts/V.

To determine the *A0* constant, we must define the relationship between the output (counts) of the seismic recording system and the input (ground motion). To do so we evaluate the complex angular frequency of the transfer functions on the imaginary axis such that

$$s = i\omega$$

to determine the velocity frequency response function

$$T_{vel-rad}(i\omega) = C_{vel-rad}F_{vel-rad}(i\omega) = C_{vel-rad}\frac{(i\omega)^2}{(i\omega)^2 + 2\beta\omega_0(i\omega) + (\omega_0)^2}$$

The normalization factors are calculated such that the modulus of the frequency-dependent $F(i\omega)$ term, in the frequency response function, multiplied by the *A0* factor is unity at the calibration frequency ω_c, or

$$A0_{vel-rad} = \frac{1}{|F_{vel-rad}(i\omega_c)|}$$

The calibration frequency, ω_c, should be within the passband of the instrument. The units of ω_c are in radians.

To determine G_s, the effect of additional resistors and the datalogger on the seismometer's generator constant, G_0, is taken into account such that

$$G_s = \frac{G_0 R_{load}}{R_t}$$

(Eaton, 1975; Healy and O'Neil, 1977).

The digitizer gain, G_d, can be determined by taking the inverse of the digitizer's bit weight, *BW,* which is in units of V/counts (sometimes provided on the digitizer calibration sheets or log files). The BW is essentially equivalent to the digitizer's least significant bit (LSB). The LSB is defined as the voltage per count.

If a gain is set on the digitizer, the effective LSB can be calculated using

$$LSB_{eff} = \frac{LSB}{GAIN}$$

Conversion Between Hz and Radian

Often sensor data sheets will have calibrated pole-zero and A0 information for each individual sensor on the sensor specification sheet. If the values are given in Hz, the values can be converted to radians using

$$Pole_{rad} = Pole_{Hz} \cdot (2\pi)$$
$$Zero_{rad} = Zero_{Hz} \cdot (2\pi)$$

$$A0_{rad} = A0_{Hz} * (2\pi)^{np-nz}$$

where np is the number of poles and nz is the number of zeros.

Seismic System Data Processing

The raw seismic data was first converted to a common SAC format. Data from Groups A, B, and C were originally in suds, cd1.1, and gcf format, respectively. Suds data was converted to SAC by creating a computer program based on Python and ObsPy, cd1.1 files were converted to SAC using the Geotech program SMARToffline, and gcf files were converted using the Guralp utilities gcfsplit and gcf2sac.

The Geospace HS-1 geophones were operated with the shunt open. The Geotech SMART-24R dataloggers with ADC Board version 06 were configured to 40 Vpp bipolar differential input range when paired with the GS-13 sensors, and configured to 5 Vpp bipolar differential when paired with the HS-1 sensors. Additional parameters can be found in Tables A1 and A2.

Pole-zero files for each instrument-datalogger combination were derived using the above methodology and applied to the raw data.

Parameter	Value
f_0	2.0 Hz
G_{0-avg}	78.74 V/m/s
m	0.023 kg
β_{0-avg}	0.61
R_{c-avg}	3800 Ω
R_s	0 Ω
$Z_{amp-HS1-S24}$	250,000 Ω
GAIN	8

Table A1. HS-1-LT geophone sensor specifications. Average values are listed by the subscript avg. These average values are input into the actual calculations since sensor specification sheets were not available for these instruments. f_0 = natural frequency of the sensor, G_0 = intrinsic sensitivity of the sensor (often also called the main coil generator constant), m = internal mass, β_0 = open circuit damping, R_c = main coil resistance, R_s = external damping resistor, $Z_{amp-HS1-S24}$ = SMART-24 datalogger input resistance, and *GAIN* = digitizer gain.

Parameter	Value
f_0	1.0 Hz
G_{0-avg}	2300 V/m/s
m	5 kg
β_{0-avg}	0.01
R_{c-avg}	9200 Ω
R_{s-avg}	111K Ω
$Z_{amp-GS13-S24}$	2M Ω
$Z_{amp-DM24}$	1M Ω
GAIN	1

Table A2. Sensor and digitizer specifications for sites with GS-13 sensors. Average values are indicated by the subscript *avg*, and are listed for informational purposes only. The true values from the sensor specification sheets are input into the actual calculations. f_0 = natural frequency of the sensor, G_0 = intrinsic sensitivity of the sensor (often also called the main coil generator constant), m = internal mass, β_0 = open circuit damping, R_c = main coil resistance, R_s = external damping resistor, $Z_{amp-GS13-S24}$ = SMART-24 datalogger input resistance, $Z_{amp-DM24}$ = DM24-S3 datalogger input resistance, and *GAIN* = digitizer gain.

Appendix B

List of Master Events

Date (UTC)	Time (UTC)	Latitude	Longitude	Depth AMSL (km)	Magnitude (Mw)
2012/10/31	02:13:05.23	43.7271	-121.3093	0.88	0.81
2012/10/31	03:58:01.23	43.7261	-121.3077	0.86	0.60
2012/10/31	17:31:25.33	43.7283	-121.3091	0.91	1.51
2012/11/01	13:38:26.95	43.7266	-121.3130	-0.33	0.75
2012/11/01	20:48:36.26	43.7282	-121.3091	0.95	1.25
2012/11/02	08:51:15.90	43.7256	-121.3072	0.02	1.23
2012/11/02	12:19:11.30	43.7294	-121.3143	-0.85	1.02
2012/11/04	01:57:21.95	43.7266	-121.3143	-0.56	0.72
2012/11/04	19:03:09.89	43.7308	-121.3114	-0.50	0.76
2012/11/09	10:30:33.30	43.7222	-121.3180	-0.57	0.83
2012/11/10	18:25:56.04	43.7276	-121.3100	-0.72	1.21
2012/11/11	04:13:18.52	43.7271	-121.3122	-0.92	0.87
2012/11/11	04:17:36.46	43.7286	-121.3077	-0.37	0.70
2012/11/13	16:50:34.91	43.7232	-121.3137	-0.71	1.16
2012/11/14	04:27:55.59	43.7258	-121.3123	-0.52	0.76
2012/11/14	07:37:01.95	43.7308	-121.3092	-0.78	0.65
2012/11/17	00:18:25.37	43.7259	-121.3113	-0.36	0.63
2012/11/17	00:18:47.16	43.7261	-121.3123	-1.04	0.32
2012/11/17	07:04:55.84	43.7219	-121.3142	-0.46	1.36
2012/11/21	05:56:42.95	43.7208	-121.3154	-0.89	0.88
2012/11/27	11:35:06.79	43.7318	-121.3203	-0.87	0.76
2012/11/29	20:31:23.47	43.7271	-121.3175	-0.70	2.04
2012/12/01	22:40:19.55	43.7272	-121.3176	-0.50	1.45
2012/12/01	22:45:22.12	43.7271	-121.3170	-0.67	1.85
2012/12/02	01:58:48.03	43.7272	-121.3098	0.70	0.71
2012/12/02	04:24:39.86	43.7270	-121.3087	0.69	0.78
2012/12/02	14:04:22.41	43.7222	-121.3150	-0.81	0.91
2012/12/02	22:37:35.00	43.7270	-121.3174	-0.48	1.33
2012/12/02	23:01:44.79	43.7207	-121.3181	-0.61	1.17
2012/12/03	03:53:51.03	43.7212	-121.3143	-0.83	1.06
2012/12/03	04:19:00.29	43.7264	-121.3153	-0.57	0.95
2012/12/03	08:17:57.40	43.7279	-121.3127	-0.56	1.52
2012/12/03	11:48:36.38	43.7266	-121.3173	-0.79	0.62
2012/12/03	13:50:52.10	43.7229	-121.3170	-0.45	0.77
2012/12/05	09:23:40.64	43.7263	-121.3115	-0.74	1.35
2012/12/05	11:18:37.08	43.7268	-121.3056	-0.21	0.92

2012/12/05	11:19:29.40	43.7268	-121.3096	-0.70	1.08
2012/12/05	16:02:12.01	43.7257	-121.3105	0.98	1.06
2012/12/06	10:39:52.40	43.7270	-121.3098	0.65	0.41
2012/12/06	17:18:46.90	43.7258	-121.3115	-0.48	0.65
2012/12/06	17:20:46.87	43.7261	-121.3106	-0.81	0.70
2012/12/06	17:23:45.15	43.7260	-121.3125	-0.75	0.49
2012/12/07	01:28:51.28	43.7321	-121.3092	-1.08	0.57
2012/12/07	04:22:57.30	43.7317	-121.3087	-1.00	0.54
2012/12/07	09:34:38.47	43.7220	-121.3171	-0.91	0.95
2012/12/07	16:41:58.16	43.7234	-121.3171	-1.15	1.82
2012/12/07	18:12:06.15	43.7225	-121.3179	-0.70	0.89
2012/12/07	18:12:46.24	43.7223	-121.3177	-0.55	0.72
2012/12/07	18:15:09.54	43.7229	-121.3171	-0.63	1.64
2012/12/07	18:15:39.85	43.7225	-121.3175	-0.41	0.73
2012/12/08	03:40:51.72	43.7240	-121.3113	-0.47	1.21
2012/12/08	03:41:53.78	43.7244	-121.3104	-0.59	1.04
2012/12/08	23:46:57.83	43.7260	-121.3113	-0.48	0.42
2012/12/09	08:07:06.37	43.7267	-121.3119	-0.56	0.45
2012/12/09	13:42:39.74	43.7306	-121.3144	-0.57	1.50
2012/12/09	16:15:18.45	43.7219	-121.3142	-0.64	1.36
2012/12/09	22:19:38.60	43.7218	-121.3159	-0.32	1.07
2012/12/10	11:14:37.37	43.7213	-121.3144	-0.61	1.07
2012/12/11	02:57:04.58	43.7302	-121.3151	-0.75	1.17
2012/12/12	05:08:56.09	43.7220	-121.3191	-0.70	0.87
2012/12/12	06:45:15.75	43.7205	-121.3157	-0.30	1.05
2012/12/12	21:53:56.46	43.7315	-121.3091	-0.94	1.25
2012/12/13	02:51:18.96	43.7214	-121.3157	-0.75	0.41
2012/12/18	23:00:08.45	43.7340	-121.3155	1.31	0.95
2012/12/19	14:41:51.66	43.7305	-121.3130	-0.50	2.34
2012/12/19	17:49:53.41	43.7312	-121.3180	0.37	2.24
2012/12/19	22:29:10.38	43.7299	-121.3163	0.61	1.22
2012/12/20	09:27:39.55	43.7278	-121.3165	-0.52	2.07
2012/12/20	14:03:32.83	43.7316	-121.3086	-0.98	1.57
2012/12/21	00:06:06.27	43.7357	-121.3100	-0.99	1.44
2012/12/21	22:20:42.79	43.7283	-121.3123	0.54	0.54
2012/12/24	00:33:57.57	43.7235	-121.3164	-0.71	1.71
2013/01/08	00:57:20.96	43.7276	-121.3197	-0.46	1.86
2013/01/08	01:00:54.89	43.7275	-121.3203	-0.64	2.10
2013/01/08	09:14:48.56	43.7274	-121.3196	-0.53	2.20
2013/02/08	02:48:28.41	43.7217	-121.3184	-0.37	2.14
2013/02/08	04:09:32.43	43.7215	-121.3192	-0.78	1.81
2013/02/18	16:59:56.20	43.7280	-121.3209	-0.47	1.92